Type-I and type-II Weyl fermions, topological depletion, and universal subleading scaling across topological phase transitions

Fadi Sun and Jinwu Ye

Type I and II Weyl fermions, Topological depletions and universal sub-leading scalings across topological phase transitions

Fadi Sun and Jinwu Ye

Department of Physics and Astronomy, Mississippi State University, P. O. Box 5167, Mississippi State, MS, 39762
Department of Physics, Capital Normal University,
Key Laboratory of Terahertz Optoelectronics, Ministry of Education,
and Beijing Advanced innovation Center for Imaging Technology, Beijing, 100048, China
Kavli Institute of Theoretical Physics, University of California, Santa Barbara, Santa Barbara, CA 93106
(Dated: May 24, 2017)

It was well established that physical quantities satisfy scaling functions across a quantum phase transition with an order parameter. It remains an open problem if there are scaling functions across a TQPT with extended Fermi surfaces (FS). Here, we study a simple system of fermions hopping in a cubic lattice subject to a Weyl type spin-orbit coupling (SOC). As one tunes the SOC parameter at the half filling, the system displays both Type I and Type II Weyl fermions and also various TQPT driven by the collision of particle-particle or hole-hole Weyl FS. At zero temperature, the TQPT is found to be third order whose critical exponents are determined. Then we investigate if the physical quantities such as specific heat, compressibility and magnetic susceptibilities satisfy any sort of scalings across the TQPT. In contrast to all the previous cases in quantum or topological transitions, we find that although the leading terms are non-universal and cutoff dependent, the sub-leading terms are non-analytic and satisfy universal scaling relations. The sub-leading scaling leads to the topological depletions which shows non-Fermi liquid corrections and $\sqrt{T}$ quantum cusps. One can also form a topological Wilson ratio from the subleading scalings of two conserved quantities such the specific heat and the compressibility. One may also interpret the Type I and Type II Weyl fermions as a TQPT driven by collision of particle-hole Weyl FS. Experimental realizations and detections in cold atom systems and materials with SOC are discussed.

I. INTRODUCTION

Quantum phase transitions with an order parameter have been under intense investigations since the experimental discovery of high temperature superconductivity. It was known that various experimental measurable physical quantities near a quantum phase transition satisfy various universal scaling functions at a finite temperature[1,2]. In an other forefront, topological phases and phase transitions without an order parameter have also been explored since the experimental observations of the quantum Hall effects[3]. Topological phenomena in various fermionic systems[4,5] have been revived since the more recent experimental realizations of a new kinds of insulators called topological insulators[6,7]. It is natural to study scaling functions across various topological phase transitions without an order parameter. There are previous efforts to derive leading scaling functions across a TQPT such as the Quantum Hall to an insulator transition in[8,9] and that driven by collisions of Dirac points in a honeycomb lattice[10]. All these TQPT can be scaled to a single point in momentum space, so conventional Renormalization group (RG), large N expansion or other methods can be applied to capture low energy critical fluctuations and derive the scaling functions.

Here, we study a simple system where free fermions hopping in a cubic lattice subject to a Weyl type of spin-orbit coupling[11]. There are experimental motivations of this model from both cold atoms and materials to be discussed in Sec.VII. As one tunes the SOC parameters at the half filling, the system displays both Type I and type II fermion and also various TQPT driven by the collision of extended particle-particle or hole-hole Weyl FS. The previous RG analysis scaled to a single Dirac point in momentum space in[8–10] do not apply to such a situation due to the low energy excitations around the extended FS. Unfortunately, the previous RG analysis[12,13] designed to deal with leading scalings around an closed and extended FS do not apply here either due to various cone singularities of the FS geometry at the TQPT. Intuitively, we do not expect the physical quantities such as specific heat, compressibility and magnetic susceptibilities satisfy any leading scalings across the TQPT. However, it is important and interesting to investigate if they satisfy any sort of scaling different from the leading scalings. At zero temperature, the TQPT is found to be a third order one whose critical exponent is determined. Then we find that in contrast to all the previous cases in quantum or topological transitions, although the leading terms in all these physical quantities are non-universal and cutoff dependent, the sub-leading terms satisfy universal scaling relations. This fact is a unique and salient feature of this kind of TQPT with extended FS reconstructions. The sub-leading scaling leads to the topological depletions (TD) which show non-Fermi liquid corrections and $\sqrt{T}$ quantum cusps. The TDs show non-analytic behaviors in the quantum critical regime which can be easily distinguished from the analytic leading terms and detected experimentally. One can also form a topological Wilson ratio from the subleading scalings of two conserved quantities such the specific heat and the compressibility. One may also interpret the Type I and Type II Weyl fermions as a TQPT driven by collision of particle-hole
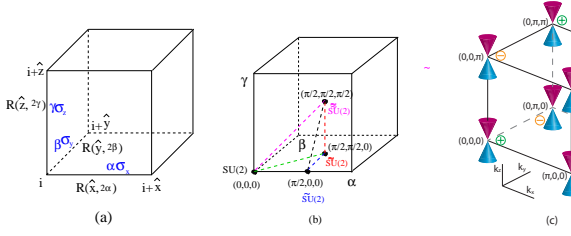
FIG. 1. (a) The non-abelian gauge fields $(\alpha\sigma_x, \beta\sigma_y, \gamma\sigma_z)$ are put on the three links in a cubic lattice. (b) The (α, β, γ) parameter space. There are one $SU(2)$ Abelian point at the origin and three more different Abelian points in the correspondingly rotated frames $\widetilde{SU}(2), \widetilde{\widetilde{SU}}(2), \widetilde{\widetilde{\widetilde{SU}}}(2)$ at the edge, face and the cubic center respectively. There are Type I Weyl fermions along the line connecting the cubic center to the edge center and Type II Weyl fermions at the face center. (c) The 8 Type I Weyl fermions with the topological charges $N_3 = \pm 1$ at $\alpha = \beta = \gamma = \pi/2$. See Fig.2 for the Weyl point explanation.

FIG. 2. A pair of Type I Weyl fermions at $(0, 0, 0)$ and (π, π, π) with opposite topological charges are turned into a particle WFS and a hole WFS respectively due to a small SOC $\alpha = \beta = \gamma = \theta$. The topological charges are conserved in the process. It is in the $q_z = 0$ cross section with the energy ϵ as the vertical axis. Note the separation between the particle and hole WFS by the FS nesting momentum $\vec{Q} = (\pi, \pi, \pi)$.

Weyl FS. We provide an intuitive classification schemes on the TQPT in terms of the collisions of FS in the particle-hole and particle-particle (or hole-hole) channel, augmented by the associated leading or sub-leading scaling functions. Some possible connections with the subleading topological entablement entropy and classical cusps in $O(3)$ Heisenberg model are briefly discussed. Some possible perspectives are outlined. Experimental realizations and detections in cold atom systems and materials with SOC are discussed.

II. TYPE I WEYL FERMIONS AS A TQPT

The Hamiltonian of fermions hopping in a cubic lattice subject to Weyl type spin-orbit coupling in Fig.1a can be written as

$$H = \sum_k h_i(\boldsymbol{k})\sigma_i, i = 0, 1, 2, 3 \tag{1}$$

where $\sigma_i = \sigma_0$ is the identity matrix, σ_i are 3 Pauli matrices and $h_0(k) = -2t(\cos\alpha\cos k_x + \cos\beta\cos k_y + \cos\gamma\cos k_z)$, $h_x(k) = 2t\sin\alpha\sin k_x, h_y(k) = 2t\sin\beta\sin k_y, h_z(k) = 2t\sin\gamma\sin k_z$. The Non-abelian gauge parameters (α, β, γ) are shown in Fig.1b. Its two energy bands are $\epsilon_\pm(k) = h_0(k) \pm h(k)$ where $h(k) = \sqrt{[h_x(k)]^2 + [h_y(k)]^2 + [h_z(k)]^2}$. At half filling $\mu = 0$, the particle and hole FS is given by:

$$\epsilon_\pm(k) = 0 \tag{2}$$

It is easy to see that the particle energy is related to that of the hole $\epsilon_+(\vec{k} + \vec{Q}) = -\epsilon_-(\vec{k})$ where $\vec{Q} = (\pi, \pi, \pi)$ is the FS nesting vector which separates the particle FS from the hole FS. It is this separation which distinguishes the TQPT in particle-particle or hole-hole from that of Type I in Fig.2 and Type II Weyl fermions in Fig.7 where
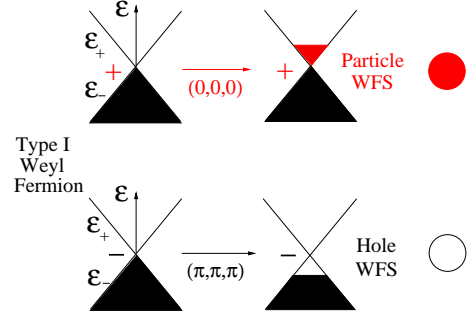
the particle WFS collides with the hole WFS. It also leads to the relation between the particle DOS and that of hole $D_+(\omega) = D_-(-\omega)$ at the half filling $\mu = 0$.

At the cubic center $(\alpha, \beta, \gamma) = (\pi/2, \pi/2, \pi/2)$ in Fig.1b, there are 8 Type I Weyl fermions located at $k_x = 0, \pi, k_y = 0, \pi, k_z = 0, \pi$ carrying the topological monopole charges $N_3 = \pm 1$ in Fig.1c. The center is the π flux (in all the three planes) Abelian point with the $\widetilde{\widetilde{\widetilde{SU}}}(2)$ symmetry in the rotated basis. It is the inversion symmetry breaking in Eq.1 which leads to their existences. Its dispersion relation $\epsilon_\pm^I(\vec{q}) = \pm\sqrt{q_x^2 + q_y^2 + q_z^2}$ leads to the dynamic exponent $z = 1$ and a vanishing DOE $D(\omega) \sim \omega^2$, so it is a semi-metal. Conventional scaling analysis with $z = 1$ in[1,2] leads to $C_v \sim T^3, \chi_u \sim T^2$ which can be easily distinguished from convention Fermi Liquid (FL) behaviors $C_v \sim T, \chi_u \sim C$. Here we focus on rich and interesting topological phase transitions along the three lines emanating from the 8 Type I Weyl fermions. We will only focus on the half filling case $\mu = 0$. Away from the center, some or all Weyl fermions will become closed particle or hole Weyl Fermi surface (WFS) shown in Fig.2. The WFS still keep the topological monopole charges $N_3 = \pm 1$ of the Weyl fermions[4]. How the WFS evolve along the three lines $\alpha = \beta = \gamma = \theta, \alpha = \pi/2, \beta = \gamma = \theta, \alpha = \beta = \pi/2, \gamma = \theta$ are shown in Fig.3,5,6 respectively. The WFS satisfy $\sum_{i=1}^8 N_{3i} = 0$ during the evolution. Extend our analysis to the doping cases with $\mu \neq 0$ and map out the global topological phase diagrams in the chemical potential μ and the SOC parameter space will be presented in subsequent works.
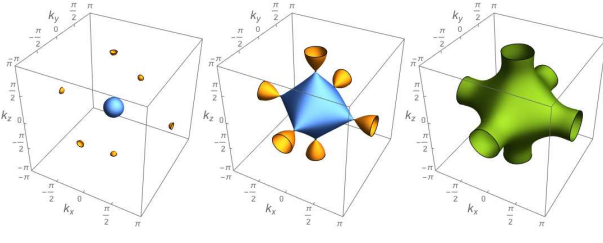
FIG. 3. The particle WFS evolves along $\alpha = \beta = \gamma = \theta$ for $\theta = 4\pi/9, \pi/3, \pi/4$. At the QCP $\theta_c = \pi/3$, the big WFS with $N_3 = 1$ (blue) hits the other 3 small WFS (yellow) with $N_3 = -1$ at 6 Fermi points at $\vec{K}_c = (\pm 2\pi/3, 0, 0), (0, \pm 2\pi/3, 0), (0, 0, \pm 2\pi/3)$. As θ increases further, it becomes a whole (green faucet tap-like) Fermi surface with the total $N_3 = 1 - 1 - 1 - 1 = -2$ charge, so it is a topological non-trivial FS. The hole WFS can be reached by shifting the particle WFS by the FS nesting vector (π, π, π).

III.   THE THIRD ORDER TQPT ALONG $\alpha = \beta = \gamma = \theta$ AT ZERO TEMPERATURE.

In this section, we focus on along the diagonal line $\alpha = \beta = \gamma = \theta$ in Fig.1b and at the half filling $\mu = 0$. How the WFS evolves along this line is shown in Fig.3. Notably, there is a TQPT driven by the collisions of the 4 WFS where the colliding 4 particle WFS takes a saddle point (cone) geometry near a Von Hove singularity $K_c = 2\pi/3$ and the critical SOC parameter $\theta_c = \pi/3$. When expanding around the VHS $K = K_c + \Delta/\sqrt{3}$ and θ_c in Fig.4, we get the particle energy spectrum:

$$\epsilon_+(\vec{q}) = -[\Delta + aq_x^2 - b(q_y^2 + q_z^2)] \qquad (3)$$

where $\Delta = \sqrt{3}(\theta_c - \theta)$ is the tuning parameter and $a = 1/2, b = 3/4 + \Delta/4$.

The DOS takes the piece-wise form:

$$D(\omega) = \begin{cases} B[\Lambda - \sqrt{\frac{-(\omega+\Delta)}{a}}], & \omega + \Delta < 0 \\ B\Lambda, & \omega + \Delta > 0 \end{cases} \qquad (4)$$

where Λ is the momentum cutoff and $B = \frac{1}{(2\pi)^2 b}$. Note the non-analytic depletion in the DOS due to the TQPT.

From the DOS, we can evaluate the ground state energy and find:

$$E \sim \begin{cases} \alpha \Delta^2 + \frac{1}{(2\pi)^2 b} \frac{2}{\sqrt{a}} \frac{2}{15} |\Delta|^{5/2} + \cdots, & \Delta < 0 \\ \alpha \Delta^2 + B_0 \Delta^3 + \cdots, & \Delta > 0 \end{cases} \qquad (5)$$

where $\cdots$ means analytical terms or higher order non-analytic terms, the α, B_0 are cutoff dependent. Only the leading non-analytic term is cutoff in-dependent and universal. It is the Δ dependence of b which leads to the background numerical value -0.77.

At the half filling $\mu = 0$, plugging the parameters $\Delta = \sqrt{3}(\theta_c - \theta), a = 1/2, b = 3/4 + \Delta/4$ into Eq.5 and taking two derivatives lead to:

$$E''(\theta, \mu = 0) \sim \begin{cases} \alpha + A_0 \sqrt{\theta - \theta_c}, & \theta > \theta_c \\ \alpha + B_0(\theta - \theta_c), & \theta < \theta_c \end{cases} \qquad (6)$$
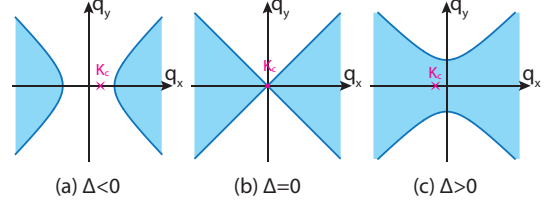

(a) Δ<0   (b) Δ=0   (c) Δ>0

FIG. 4. The FS geometry near the TQPT driven the particle-particle WFS collision at $K_c = \pi - \theta_c, \theta_c = \pi/3$ in the $q_z = 0$ cross section. The $K = \pi - \theta = K_c + \Delta/\sqrt{3}$ is the VHS. The hole-hole WFS collision is similar by changing the shaded regime to a vacuum.

where the exponents $\nu_- = 1/2, \nu_+ = 1$ are universal and the coefficient $A_0 = 0.18856$ is cutoff independent and stands for the universal contributions from a single cone of the TQPT in Fig.4. While B_0 is not universal and cut-off dependent.

At the half filling $\mu = 0$, there are 6 particle and 6 hole WFS colliding at the same time. So in the second derivatives of the total ground state energy: $A = 12A_0 = 2.262$.

We performed numerical calculations on the ground state energy in the BZ as shown in the Appendix A.

$$E_n''(\theta, \mu = 0) \sim \begin{cases} -0.77 + A_n(\theta - \theta_c)^{\nu_+}, & \theta > \theta_c \\ -0.77 + B_n(\theta - \theta_c)^{\nu_-}, & \theta < \theta_c \end{cases} \qquad (7)$$

where the numerical exponents $\nu_+ = 0.5 \pm 0.05, \nu_- = 1.0 \pm 0.05$ match the analytical values $\nu_+ = 1/2, \nu_- = 1$ well, the numerical coefficient $A_n = 2.19$ is also very close to the analytical value $A = 2.262$ achieved above.

IV.   SUB-LEADING SCALING FUNCTIONS ACROSS THE THIRD TQPT AT A FINITE T

It was established[1,2] that near a quantum phase transition at zero temperature, the experimental measurable physical quantities such as single particle Green functions, specific heat, compressibility, magnetic susceptibilities, etc should satisfy scaling functions. However, there are always low energy excitations around the WFS on both sides of the TQPT in Fig.4. It becomes problematic to apply the scaling analysis near a quantum phase transition with an order parameter to such a TQPT. Unfortunately, the previous RG analysis[12,13] designed to deal with leading scalings around an extended FS do not apply here due to the cone singularity of the FS geometry in Fig.4. From Eq.3, intuitively, one can still define the dynamic exponent $z = 2$ with respect to the cone singularity. However, its physical meaning should be quite different from that defined in the QPT with an order parameter and symmetry breaking[1,2] and need to be carefully examined. Indeed we show that despite the leading terms in all these physical quantities are cutoff dependent and non-universal, the subleading terms do satisfy universal scaling with $z = 2$ which lead to non-analytic

therefore non-Fermi liquid corrections to the leading analytic terms. They always take the opposite sign to the leading term, therefore can be called topological depletions.

Because $z = 2$, one can apply the scaling analysis in[10] here to write down the sub-leading scaling function for the specific heat and the uniform compressibility $\kappa_u = \chi^{00}(\vec{q} \to 0, \omega = 0)$ for a single particle-particle (or hole-hole) cone in Fig.4:

$$C_v = \frac{\pi^2}{3} B k_B (k_B T) \Lambda - \frac{B k_B (k_B T)^{3/2}}{\sqrt{a}} \Psi_i(\frac{|\Delta|}{k_B T}) \quad (8)$$

$$\kappa_u = \frac{1}{2} B \Lambda - \frac{B (k_B T)^{1/2}}{\sqrt{a}} \Omega_i(\frac{|\Delta|}{k_B T})$$

where $i = 1, 2$ stands for the two sides of the transitions $\Delta < 0$ and $\Delta > 0$ in Fig.4 and Fig.8.

Note the first term is the leading term, proportional to the frequency (or energy) cutoff Λ and non-universal. while the second term is the sub-leading term, independent of the frequency (or energy) cutoff Λ and a universal function of the scaling variable $s = \frac{|\Delta|}{k_B T}$. Due to the opposite sign between the two terms, the universal sub-leading term can be interpreted as the topological depletion coming from the TQPT.

The general form of the two scaling functions $\Psi_i(x)$ and $\Omega_i(x)$ are evaluated in the appendix B. Here, we only list the topological depletions in the three limiting regimes in Fig.8 for the specific heat

$$C_v^{TD} = \begin{cases} -\frac{\pi^2}{3} \frac{B}{\sqrt{a}} k_B^2 T \sqrt{|\Delta|}, & \Delta \ll -k_B T \\ -2.88201 \frac{B}{\sqrt{a}} k_B^{5/2} T^{3/2}, & |\Delta| \ll k_B T \\ -\frac{\sqrt{\pi}}{2} \frac{B k_B^{1/2}}{\sqrt{a}} \frac{\Delta^2}{\sqrt{T}} e^{-\frac{\Delta}{k_B T}}, & \Delta \gg k_B T \end{cases} \quad (9)$$

and for the uniform compressibility:

$$\kappa_u^{TD} = \begin{cases} -\frac{B}{\sqrt{a}} \sqrt{|\Delta|}, & \Delta \ll -k_B T \\ -0.536077 \frac{B k_B^{1/2} T^{1/2}}{\sqrt{a}}, & |\Delta| \ll k_B T \\ -\frac{\sqrt{\pi}}{2} \frac{B k_B^{1/2} T^{1/2}}{\sqrt{a}} e^{-\frac{\Delta}{k_B T}}, & \Delta \gg k_B T \end{cases} \quad (10)$$

One can see both topological depletions are non-analytic only in the QC regime in Fig.8. While, essentially no depletion when $\Delta \gg T$ and a constant $\sqrt{|\Delta|}$ depletion when $-\Delta \gg T$ which can be absorbed to the leading FL contribution anyway. This fact make their experimental detections feasible (see Sec.7).

One can also form the topological Wilson ratio $R_W^{TD}\left(\frac{|\Delta|}{k_B T}\right) = \frac{k_B^2 T \kappa_u^{TD}}{C_v^{TD}}$ whose values in the three regimes are:

$$R_W^{TD} = \begin{cases} 3/\pi^2 & \Delta \ll -k_B T \\ 0.186, & |\Delta| \ll k_B T \\ \left(\frac{k_B T}{\Delta}\right)^2, & \Delta \gg k_B T \end{cases} \quad (11)$$
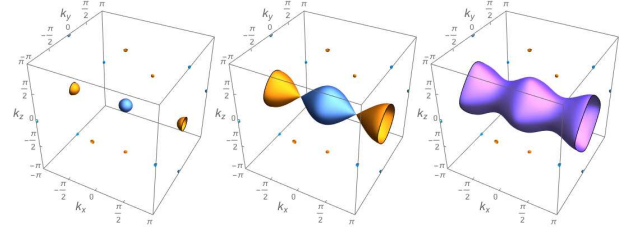

FIG. 5. The particle WFS evolves along $\alpha = \pi/2, \beta = \gamma = \theta$ for $\theta = 4\pi/9, \pi/3, \pi/4$. The end point $\theta = 0$ (not shown) is the 0 flux (in all the three planes) Abelian point with the $\tilde{S}U(2)$ symmetry in the rotated basis in Fig.1b. At $\theta_c = \pi/3$, the WFS with $N_3 = 1$ hits the one with $N_3 = -1$ at the two Fermi points at $\vec{K}_c = (\pm\pi/2, 0, 0)$. As θ decreases further, it becomes a whole Fermi surface (violet vase) with the total $N_3 = 1 - 1 = 0$ charge, so it is topologically trivial FS. The rest 4 Type I Weyl fermions remain intact through the TQPT. This should be in a different class of TQPT than in Fig.3. The co-existence of the 4 Type I Weyl fermions and the TQPT of WFS is one of the new features along this line. The hole WFS can be reached by shifting the particle WFS by one of the two FS nesting vectors $(0, \pi, \pi), (\pi, \pi, \pi)$.

which is even independent of a and b characterizing the shape of the cone in Fig.8. In fact, it is also independent of how many cones are participating in the TQPT[16], so universal for all the TQPTs in Fig.3,5,6.

As shown in the appendix B, due to the $[C_4 \times C_4]_D$ symmetry at $\alpha = \beta = \gamma$, the topological depletions of the magnetic susceptibility $\chi^{xx}(T) = \chi^{yy}(T) = \chi^{zz}(T) = \frac{1}{3}\chi^{00}(T)$ also satisfy the sub-leading scaling Eq.10.

V. THE 3RD ORDER TQPT ALONG THE LINE $\alpha = \pi/2, \beta = \gamma = \theta$ AND CO-EXISTENCE OF FOUR TYPE I WEYL FERMIONS

At half filling $\mu = 0$, 2 particle WFS and 2 hole WFS collide at the same time at $\vec{K}_c = (\pi/2, 0, 0)$ and $\theta_c = \pi/3$. The dispersion near $K_c = \pm\pi/2, \theta_c = \pi/3$ can also be written as Eq.3 where $\Delta = \sqrt{3}(\theta_c - \theta), a = 1/2, b = 5/8 - \Delta^2/8$. Using Eq.6, we find $A_0 = 0.2263$, then the 2 particle WFS and 2 hole WFS contribute to $A = 4A_0 = 0.90$. Similarly, the subleading scaling function in Eq.9 and Eq.10 need also multiply by 4, but the topological Wilson ratio Eq.11 remains identical. As shown in appendix B, due to the non-conservation of the spins, only the sum over the spin components $\sum_i \chi^{ii}(T) = \kappa_u$ in the magnetic susceptibilities satisfy the sub-leading scaling Eq.10.

We also performed numerical calculation in the whole BZ:

$$E_n''(\theta, \mu = 0) \sim \begin{cases} -0.224 + A_n(\theta - \theta_c)^{\nu_+}, & \theta > \theta_c \\ -0.224 + B_n(\theta - \theta_c)^{\nu_-}, & \theta < \theta_c \end{cases} \quad (12)$$

where $A_n = 0.861$ is quite close to the analytic value $A = 4A_0 = 0.90$.

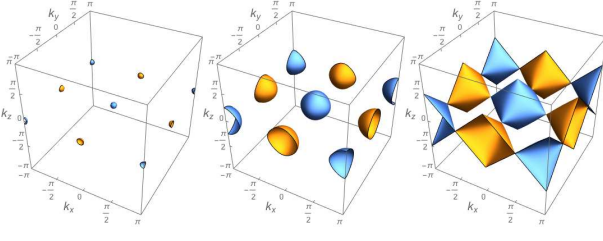### 1. Coexistence of 4 Type I Weyl fermions

FIG. 6. The particle WFS evolves along $\alpha = \beta = \pi/2, \gamma = \theta$ for $\theta = 4\pi/9, \pi/4, 0$. The TQPT happens at the end point $\theta_c = 0$ where it becomes a corner-sharing octahedron. The hole WFS can be reached by shifting the particle WFS by one of the 4 FS nesting vectors $(0,0,\pi), (\pi,0,\pi), (0,\pi,\pi), (\pi,\pi,\pi)$. There are also 8 straight Type II Weyl fermions at $\theta_c = 0$ shown in Fig.7.

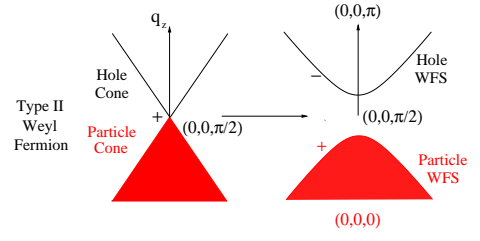FIG. 7. A type II Weyl fermion at $(0,0,\pi/2)$ and $\theta_c = 0$ in Fig.6 can be viewed as a TQPT of a particle WFS and a hole WFS. It is in the cross section of $q_x = 0$ or $q_y = 0$ with q_z as the vertical axis. Under a small SOC $\alpha = \beta = \pi/2, \gamma = \theta$, it splits into a Type I particle WFS with a charge 1 centered at $(0,0,0)$ and a Type I hole WFS with a charge -1 centered at $(0,0,\pi)$.

As shown in Fig.5, there are also 4 Type I Weyl fermions located at $(0,0,\pi), (0,\pi,0), (\pi,0,\pi), (\pi,\pi,0)$ with the anisotropic dispersion $\epsilon_\pm^I = -[\frac{1}{2}(q_z^2 - q_y^2) \mp \sqrt{q_x^2 + \sin^2\theta(q_y^2 + q_z^2)}]$. They reman intact through the TQPT, so just act as 4 spectators. From the simple scaling analysis with $z = 1$, their contributions to the specific heat is $C_v \sim T^{d/z} \sim T^3$ which is analytic and subleading to the topological analytic depletion $C_v \sim T^{d/z} \sim T^{3/2}$ in the QC regime due to the third order TQPT. Furthermore, it can not be distinguished from the analytic T^3 FL corrections. However, they do contribute to the surface Fermi arcs and associated chiral anomalies in the transport properties. How the TQPT in the bulk in Fig.5 interfere with the surface Fermi arcs need to be investigated in a separate publication.

VI.   THE 5TH ORDER TQPT ALONG THE LINE $\alpha = \beta = \pi/2, \gamma = \theta$ AND THE 8 TYPE II WEYL FERMIONS.

How the FS evolves along this line is shown in Fig.6. As shown in Fig.6, there is a TQPT at the π flux (in XY plane) Abelian ending point $\theta_c = 0$ with the $\tilde{\tilde{SU}}(2)$ symmetry in the rotated basis in Fig.1b. At half filling $\mu = 0$, all the 4 particle WFS and 4 hole WFS collide at the same time at $\theta_c = 0$. Near $\vec{K}_c = (\pi/2, 0, 0), \theta_c = 0$, the dispersion can also be written as Eq.3 where $\Delta = -\theta^2/2, a = 1/2, b = 1/2 + \Delta/2$. Note the quadratic dependence of Δ on the SOC tuning parameter θ. Plugging these parameters into Eq.5, we find

$$E \sim \frac{1}{15\pi^2}|\theta|^5 + \cdots \tag{13}$$

where $\cdots$ means leading analytical terms. Taking 5 derivatives to get rid of the leading analytic terms leads to

$$\frac{d^5 E}{d\theta^5} \sim \frac{8}{\pi^2} sgn\theta \tag{14}$$

It shows that the transition is a 5th order one. Because all the 4 particle WFS and 4 hole WFS collide at the same time, $A = 8A_0 = \frac{64}{\pi^2}$. Similarly, the subleading scaling function in Eq.9 and Eq.10 need also multiply by 8, but the topological Wilson ratio Eq.11 remains the same.

1. Type II Weyl fermions at $\alpha = \beta = \pi/2, \theta = 0$ as a TQPT

One new feature at the TQPT $\theta_c = 0$ is that in addition to the particle-particle and hole-hole WFS collisions, the particle WFS also touches the hole WFS shown in Fig.6 and 7, such a cone structure between the particle WFS and the hole WFS is nothing but a special case of the type II Weyl fermions discussed in[24]. Shown in Fig.7 is essentially a 3d version of 2d Dirac fermions. In 2d case, it was known[15] that there are 4 Dirac fermions at $\alpha = \beta = \pi/2$ with topological charges $1, -1, 1, -1$ at the 4 Time-reversal invariant momenta $(0,0), (\pi,0), (\pi,\pi), (0,\pi)$. Now adding the third dimension without putting any SOC along it will change the 4 Dirac fermions into the 8 Type II Weyl fermions at the 8 momenta $(0,0,\pm\pi/2), (\pi,0,\pm\pi/2), (\pi,\pi,\pm\pi/2), (0,\pi,\pm\pi/2)$ shown in Fig.6. Their topological charges are determined by the projections onto the (k_x, k_y) plane, independent of the k_z component, so still given by $1, -1, 1, -1$ at the 4 projections on the (k_x, k_y) plane: $(k_x, k_y) = (0,0), (\pi,0), (\pi,\pi), (0,\pi)$.

Without losing any generality, we look at the Type II Weyl fermion's dispersion at $(0,0,\pi/2)$:

$$\epsilon_\pm^{II}(\vec{q}) = -[-q_z \mp \sqrt{q_x^2 + q_y^2}] \tag{15}$$

where the $\pm$ corresponds to the particle and hole WFS shown in Fig.7. At $\mu = 0$, taking $-$ sign leads to the particle WFS $-q_z \geq \sqrt{q_x^2 + q_y^2}$ which takes a cone structure near $(0,0,\pi/2)$. Taking $+$ sign leads to the hole WFS $q_z \geq \sqrt{q_x^2 + q_y^2}$ which also takes a cone structure above the particle cone shown in Fig.7. Now putting the SOC $\gamma = \theta$ along the third direction, any small θ immediately opens gap to both the particle WFS
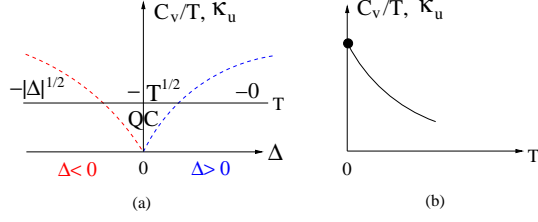
FIG. 8. Experimental signatures of the topological depletions and sub-leading scalings (a) The specific heat C_v/T and the compressibility κ_u at a given T shows a non-analytic $\sqrt{T}$ depletion in the QC regime. The FS geometry in the three regimes are shown in Fig.4. (b) The quantum $\sqrt{T}$ cusps in C_v/T and κ_u in the QC regime in (a) as T lowers. From the ratio of the coefficients of the $\sqrt{T}$ in the two quantities, one may also measure the universal Topological Wilson ratio R_W^{TD}.

$-q_z \geq \sqrt{\theta^2 + q_x^2 + q_y^2}$ near $(0,0,0)$ and the hole WFS $q_z \geq \sqrt{\theta^2 + q_x^2 + q_y^2}$ near $(0,0,\pi)$ with the dynamic exponent $z = 1$ in Fig.7. At the same time, the 4 particle WFS split with the form Eq.3 with the dynamic exponent $z = 2$. The 4 hole WFS also split at the 4 FS nesting momenta. When θ gets close to $\pi/2$, then the particle and the hole WFS shrink to a small sphere with $q_x^2 + q_y^2 + q_z^2 = (\pi/2 - \theta)^2$ shown in Fig.2. At $\theta = \pi/2$, they shrink to Type I Weyl fermion shown in Fig.1. Although type I fermion is a semi-metal, while in the Type II Weyl fermion, both the extended particle and hole WFS add to contribute to a finite DOS $D(\omega) \sim \Lambda^2 - \alpha\omega^2$ with a possible topological depletion in DOS $\sim \alpha\omega^2$, so it is a metallic phase[26]. For tilted Type II Weyl fermions in[24], $\alpha > 0$. While for the special straight Type II Weyl fermions in Fig.7, $\alpha = 0$.

From the simple scaling analysis, the 8 Type II Weyl fermions with $z = 1$ contribute to the specific heat $C_v^D \sim \alpha T^3$ which is subleading to the topological depletion $C_v^D \sim T^{3/2}$ due to the 5th order TQPT in the QC regime. In fact, as said above, for the straight Type II Weyl fermions, even the coefficient $\alpha = 0$, so it does not even have a topological depletion to C_v^D, χ_u^D.

VII. EXPERIMENTAL REALIZATIONS AND DETECTIONS IN COLD ATOMS AND MATERIALS

The Hamiltonian Eq.1 of free fermions hopping in a cubic lattice subject to a Weyl type of spin-orbit coupling can be achieved by loading cold atoms in a cubic optical lattice. Indeed, recently, 2d SOC has been experimentally implemented in the fermion ^{40}K gas[29,30]. Soon after, using an optical Raman lattice scheme, the authors in the experiment[32] realized the Rashba SOC of spinor bosons with tunable (α, β) in a square lattice. An optical lattice clock scheme[31] was proposed to generate a 2d SOC in an optical lattice, it has the advantages to suppress the possible heatings issue. Most recently, by using the most magnetic fermionic element dysprosium to eliminate the heating due to the spontaneous emission, the authors in[33] created a long-lived SOC gas of quantum degenerate atoms. The long lifetime of this weakly interacting SOC degenerate Fermi gas will facilitate the experimental study of quantum many-body phenomena manifest at longer time scales. The heating issues with fermions may be more serious than those with spinor bosons. However, the TQPT in Fig.3,5,6 are for non-interacting fermions, they are essentially single particle properties, so the heating issues should be manageable in current cold atom experiments with fermions.

Of course, any experiments are performed at finite temperatures which are controlled by the topological phase transitions at $T = 0$ in Fig.3,5,6. The TQPTs do not survive at finite $T > 0$, but become the 3 crossover regimes shown in Fig.8. The crossover temperature can be estimated as $T \sim \Delta \sim t \sim 3nK$ which is easily experimental reachable with the current cooling techniques[34,35], so the $\sqrt{T}$ quantum cusp behaviors in C_v/T and κ_u, the universal Topological Wilson ratio in Fig.8 could be detected by the specific heat measurements[36,37], In-Situ measurements[38] and the compressibility κ measurements[37]. The change of the FS topology across the TQPT in Fig.3,5,6 and in the Type I Weyl fermions in Fig.2 and Type II Weyl fermions in Fig.7 can be monitored by the momentum resolved interband transitions[39] and the band mapping technique developed in[32].

As shown in Fig.3,5,6, Type I fermions are quite common and robust in this simple SOC model. However, the Type II fermions seem quite restricted, also only straight Type II fermions different than the tilted Type II proposed in[24] can be realized. Subleading scaling functions in Eq.9 and 10 can be easily extended to the Type II Weyl fermions with $z = 1$ in these materials. Unfortunately, the topological depletion $\sim T^3$ is analytic, can not be distinguished from the FL corrections which are also T^3. As said above, there is no such topological depletion for the straight Type II fermions. Type I Weyl fermions have been discovered in several materials[18–22]. Type II Weyl fermions[24] seem also have been found in a few materials, although there are still quite controversial experimental interpretations on the number of bulk type II Weyl fermions and associated surface Fermi arcs[27,28]. Topological Lifshitz transitions happen in all these Type I and Type II Weyl fermion materials. Although they may not be described precisely by the Hamiltonian Eq.1, they should be in the same topological classes as those in Fig.3,5,6. So the results achieved in this paper should also apply to the Topological Lifshitz transitions in these non-interacting or weakly interacting materials.

VIII.   DISCUSSIONS AND CONCLUSIONS

We may classify the FS topologies at the half filling in terms of topological phase transitions and associated leading or sub-leading scaling functions. There are two kinds of TQPT: (1) the first one is between particle and hole which leads to Type I and Type II fermions. (a) Type I Weyl fermions are relativistic, have closed either particle or hole FS with the DOS $D(\omega) \sim \omega^2$ and satisfy leading analytic scaling with the dynamic exponent $z = 1$. (b) Type II Weyl fermions are non-relativistic, have extended open particle and hole FS with the DOS $D(\omega) \sim \Lambda^2 - \alpha\omega^2$ and satisfy sub-leading analytic scaling with the dynamic exponent $z = 1$. (2) The second one is the TQPT between particle and particle (or hole and hole) through a cone singularity, has extended FS on both sides with the DOS given in Eq.4 and satisfy sub-leading non-analytic scaling with the dynamic exponent $z = 2$. Our preliminary results away from half filling shows there are new classes of TQPT with anisotropic dynamic exponents[43]. Of course, at sufficiently large μ, there is a quadratic band touching through a closed hole FS with the DOS $D(\omega) \sim \sqrt{\omega}, \omega > 0; D(\omega) = 0, \omega < 0$. It leads a metal to BI transition which satisfies a leading non-analytic scaling with dynamic exponent $z = 2$. The results will be presented in a subsequent publication. It would be also interesting to look at the physical classification here from formal K theory classification. However, so far, the K theory classification only assumes the translational symmetry, but ignore the constraints from crystalline symmetries which take the spin-orbital coupled crystalline symmetries in Eq.1.

Eq.9 and 10 take a similar form to the topological entanglement entropy[44]: $S = \alpha L - \gamma$ where the first term is the leading non-universal term proportional to the length between the boundary of the two entangled regimes A and B. While the second term is the sub-leading term, independent of the boundary and universal called topological entanglement entropy $\gamma = \log D$ where D is quantum dimension D (which is a counter-part of the dynamic exponent z here). There is also a relative minus sign between the two terms ! This suggests that the form may be a general scaling structure across a TQPT, in sharp contrast to the conventional leading scaling across a conventional QPT with an order parameter and associated symmetry breaking.

The subleading scaling behaviors in the specific heat in Eq.9 remind the specific heat near the finite temperature phase transition of the classical $O(3)$ Heisenberg model[45] $C_v \sim C - b_0 t^{-\alpha}$ where $t = |(T - T_c)/T_c|, b_0 > 0$ and $\alpha \sim -0.1$. So the specific heat will show a maximum classical cusp near T_c. This cusp has been precisely detected in specific heat experiments. This fact has also been used to determine the Anomalous Hall effect near the finite temperature phase transition in[46]. Here the quantum $\sqrt{T}$ cusp behavior in the QC regime near $T = 0$ in Fig.8 is due to the TQPT at $(T = 0, \Delta = 0)$. So the mechanism of the quantum cusp discovered in this paper is completely different than that of the classical cusp.

As shown in Fig.3,5,6, Type I fermions are quite common in this simple model. In contrast to the Weyl Semi-metals in materials[18–22] which have only 2 (or 4) Weyl points if the Time reversal (or Inversion) symmetry is broken. Here there are 8 and 4 Weyl points in Fig.1c and Fig.5 respectively due to the Inversion symmetry breaking. The present paper focused on the TQPTs in the bulk. Taking a slab geometry with two surfaces (in real space) parallel to the $(1, 1, 1)$ direction, every Fermi arc connects one $+1$ to one -1 monopole, so it may be interesting to investigate how the Fermi arcs in the two surfaces connect the projections of the 8 or 4 Weyl points onto the two surfaces and monitor how the Fermi-arcs reconstruct across the TQPT in the bulk in Fig.3 and Fig.5. While 8 Type II fermions seem quite restricted, are only realized at the π flux in abelian point $\alpha = \beta = \pi/2, \gamma = 0$ in Fig.6. It remains unknown if there is a well defined surface Fermi-arcs associated with these 8 straight Type II fermions.

In terms of scaling functions, the TQPT in Fig.3,5,6 should all be in the same universality class. The topological Wilson ratio is even identical. However, the main difference is that the WFS is still topologically non-trivial carrying the topological charge $N_3 = -2$ after the TQPT in Fig.3, but becomes trivial in Fig.5 and 6. It seems the scaling functions near a single cone may not reflect the total topological charges carried by the WFS. Different TQPT may be described by the same set of scaling functions. However the total coefficient A does depend on the global topology of the WFS which is related to N_3.

Due to the vanishing of DOS at the Type I Weyl point, a weak interaction is irrelevant. But due to the extended FS at the Type II Weyl point and the particle-particle or hole-hole TQPT point, any weak interaction is relevant. Following Ref.[14,15,40,41], it is important to look at the effects of both positive U and negative U. For example, for $U > 0$ and away from half filling, due to the $N_3 = -2$ in Fig.3, depending on the signs of pairing amplitudes on different parts of WFS, it may lead to new TR invariant topological superfluids with an associated Majornan surface mode[7].

Acknowledgements

Appendix A: Numerical evaluation of zero temperature universal amplitude and critical exponents in the TPTs.

The Ground-state energy along the line $\alpha = \beta = \gamma = \theta$ is calculated as

$$E_{\mathrm{GS}}(\theta) = \frac{1}{(2\pi)^3} \int_{\mathbf{k}\ \mathrm{filled}} d\mathbf{k}[\epsilon_+(\mathbf{k};\theta) + \epsilon_-(\mathbf{k};\theta)] \quad \text{(A1)}$$
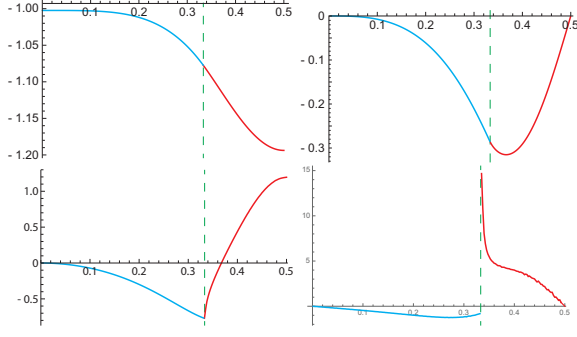
FIG. 9. The ground-state energy density and its derivatives on the lattice versus the SOC parameter θ/π. (a) The ground-state energy (b) It's first-order derivative, (c)It's second-order derivative (d)It's third-order derivative. So the TPT at $\theta_c = \pi/3$ is a third order one.

whose Numerical results are list in 9.

It is obvious that when $\theta < \theta_c$, $E''(\theta) \sim (\theta - \theta_c)$. But when $\theta > \theta_c$, it should be $E''(\theta) \sim (\theta - \theta_c)^{\nu_+}$ with some value $\nu_+ < 1$. The best fits leads to Eq.M6 with the coefficient $A_n = 2.19$ and the critical exponent $\nu_+ = -(0.50 \pm 0.05)$ which match the analytic values well.

We also performed similar calculations along the other two lines $\alpha = \pi/2, \beta = \gamma = \theta$ and $\alpha = \beta = \pi/2, \gamma = \theta$ and also found the numerical values match the analytic ones precisely.

Appendix B: Evaluations of Finite Temperature universal subleading scaling functions across a TPT.

The Internal energy is

$$U = \int_{-\infty}^{\infty} d\omega \frac{D(\omega)\omega}{e^{\frac{\omega}{k_B T}} + 1}, \tag{B1}$$

which leads to the specific heat:

$$C_v = \frac{\partial U}{\partial T} = k_B \int_{-\infty}^{\infty} d\omega D(\omega) \frac{e^{\frac{\omega}{k_B T}}}{(e^{\frac{\omega}{k_B T}} + 1)^2} \frac{\omega^2}{(k_B T)^2} \tag{B2}$$

Plugging in the DOS in Eq.M3 leads to the first equation in the scaling form Eq.M7 with the scaling variable $s = \frac{|\Delta|}{k_B T}$ where

$$\Psi_1(s) = \int_0^s dx \frac{\sqrt{s-x} x^2 e^x}{(e^x+1)^2} + \int_0^\infty dx \frac{\sqrt{s+x} x^2 e^x}{(e^x+1)^2},$$
$$\Psi_2(s) = \int_s^\infty dx \frac{\sqrt{x-s} x^2 e^x}{(e^x+1)^2} \tag{B3}$$

However, the compressibility and magnetic susceptibility involve Hamiltonian, not just DOS. From Eq.M1, one can get the fermion Green function:

$$G(i\omega, k) = [i\omega - H_k]^{-1} = \sum_{s=\pm} \frac{P_s(k)}{i\omega - \epsilon_s(k)} \tag{B4}$$

where $P_s = \frac{1}{2}\left[\sigma_0 + s \sum_i \frac{h_i}{h}\sigma_i\right]$ is the projection operators onto the particle-hole bands $s = \pm$.

The dynamic density-spin susceptibility is

$$\chi^{\mu\nu}(q, i\omega_n) = -k_B T \sum_{k,i\nu} \text{Tr}[G(i\omega_n + i\nu_n, k')\sigma^\mu$$
$$\times G(i\nu_n, k)\sigma^\nu] \tag{B5}$$

where $k' = k + q$.

Working out the sum over the Matsubara frequency leads to

$$\chi^{\mu\nu}(q, i\omega_n) = -\sum_{k,s,s'} M_{ss'}^{\mu\nu}(k,k') \frac{f_{sk} - f_{s'k'}}{i\omega_n - \epsilon_{k'}^{s'} + \epsilon_k^s} \tag{B6}$$

where the Fermi distribution function $f_{sk} = f(\epsilon_k^s)$ and $M_{ss'}^{\mu\nu}(k,k') = \text{Tr}[P_s(k)\sigma^\mu P_{s'}(k')\sigma^\nu]$.

In the static limit, we have

$$\lim_{q\to 0} \frac{f_{sk} - f_{s'k'}}{\epsilon_k^s - \epsilon_{k+q}^{s'}} = \delta_{ss'} \frac{\partial f(\epsilon)}{\partial \epsilon} + \delta_{s,-s'} \frac{f_{sk} - f_{s'k}}{2sh(k)} \tag{B7}$$

and $\lim_{q\to 0} M_{ss'}^{\mu\nu}(k,k') = M_{ss}^{\mu\nu}(k,k)\delta_{ss'}$ which is evaluated as:

$$M_{ss}^{\mu\nu}(k,k) = \begin{pmatrix} 1 & s\frac{h_x}{h} & s\frac{h_y}{h} & s\frac{h_z}{h} \\ s\frac{h_x}{h} & \frac{h_x^2}{h^2} & \frac{h_x h_y}{h^2} & \frac{h_x h_z}{h^2} \\ s\frac{h_y}{h} & \frac{h_x h_y}{h^2} & \frac{h_y^2}{h^2} & \frac{h_y h_z}{h^2} \\ s\frac{h_z}{h} & \frac{h_x h_z}{h^2} & \frac{h_y h_z}{h^2} & \frac{h_z^2}{h^2} \end{pmatrix}, \tag{B8}$$

Because the particle and hole WFS collide at momenta differing by $\vec{Q} = (\pi, \pi, \pi)$, so in extracting non-analytic contributions, one can drop the mixing between Particle and hole WFS and focus on just one collision cone between the P-P or H-H WFS. Then a single cone compressibility is:

$$\kappa_u(T) = \chi^{00}(T) = -\int_{-\infty}^{+\infty} d\omega D(\omega) \frac{\partial}{\partial \omega} \frac{1}{e^{\frac{\omega}{k_B T}} + 1} \tag{B9}$$

Plugging in the DOS in Eq.M3 leads to the second equation in the sub-leading scaling form Eq.M7 where

$$\Omega_1(s) = \int_0^s dx \frac{\sqrt{s-x} e^x}{(e^x+1)^2} + \int_0^\infty dx \frac{\sqrt{s+x} e^x}{(e^x+1)^2},$$
$$\Omega_2(s) = \int_s^\infty dx \frac{\sqrt{x-s} e^x}{(e^x+1)^2} \tag{B10}$$

From Eq.B8, one can also read the single cone spin susceptibility:

$$\chi^{ij}(T) = -\int d^3k \frac{h_i h_j}{h^2} \frac{\partial}{\partial \omega} \frac{1}{e^{\frac{\omega}{k_B T}} + 1}\Big|_{\omega = \omega_s(k)}, \tag{B11}$$

where $i, j = x, y, z$.

Since h_i is odd function of k, we have $\chi^{ij}(T) = \delta_{ij}\chi^{ii}(T)$. Using the identity $h^2 = h_x^2 + h_y^2 + h_z^2$, we get

the following sum rule for the sub-leading scaling which holds for any (α, β, γ):

$$\sum_i \chi^{ii}(T) = \kappa_u \qquad (B12)$$

Indeed, similar to the theoretical evaluations and experimental detections of the coherence length in a SOC

system[25], because the spin is not conserved, so we only expect the average over all the spin components satisfy the sub-leading scalings.

However, the enlarged $[C_4 \times C_4]_D$ symmetry at $\alpha = \beta = \gamma = \theta$ dictates

$$\chi^{xx}(T) = \chi^{yy}(T) = \chi^{zz}(T) = \frac{1}{3}\chi^{00}(T) \qquad (B13)$$

which also satisfies the sub-leading scaling individually.

[1] S. Sachdev and J. Ye ; Universal quantum-critical dynamics of two-dimensional antiferromagnets, Phys.Rev.Lett. 69, 2411 (1992); A. V. Chubukov, S. Sachdev, and J. Ye, *Theory of two-dimensional quantum Heisenberg antiferromagnets with a nearly critical ground state*, Phys. Rev. B **49**, 11919(1994).

[2] S. Sachdev, *Quantum Phase transitions*, (2nd edition, Cambridge University Press, 2011).

[3] X.G. Wen and Q. Niu, Phys. Rev. B41, 9377 (1990); Wen, X. G. Quantum Field Theory of Many-body Systems (Oxford University Press, 2004).

[4] Volovik, G. E. The Universe in a Helium Droplet (Oxford University Press, USA, 2003).

[5] Volovik, G. E. arXiv:1701.06435; arXiv:1606.08318; K. Zhang and Volovik, G. E. arXiv:1604.00849. Note that these preprints focused on the topological invariants across various topological phase transitions, so are complementary to the present work.

[6] M. Z. Hasan and C. L. Kane, Colloquium: Topological insulators, Rev. Mod. Phys. **82**, 3045 (2010).

[7] X. L. Qi and S. C. Zhang, Topological insulators and superconductors, Rev. Mod. Phys. **83**, 1057 (2011).

[8] Jinwu Ye and S. Sachdev, The effects of Coulomb interaction on Quantum Hall critical points of systems in a periodic potential, Phys. Rev. Lett. 80, 5409 (1998).

[9] Jinwu Ye, The effects of weak disorders and Coulomb interaction on Quantum Hall critical points, Phys. Rev. B60, 8290 (1999).

[10] Fa-Di Sun, Xiao-Lu Yu, Jinwu Ye, Heng Fan, W. M. Liu, Topological Quantum Phase Transition in Synthetic Non-Abelian Gauge Potential: Gauge Invariance and Experimental Detections, Scientific Reports 3, 2119 (2013).

[11] Shang-Shun Zhang, Jinwu Ye, Wu-Ming Liu, Itinerant magnetic phases and Quantum Lifshitz transitions in repulsively interacting spin-orbit coupled Fermi gas, Phys. Rev. B 94, 115121 (2016).

[12] R. Shankar, Renormalization-group approach to interacting fermions, Rev. Mod. Phys. 66, 129 (1994) - Published 1 January 1994

[13] J. Ye and S. Sachdev, Superconducting,metallic,and insulating phases in a model of CuO_2 layers, Phys. Rev. B 44, 10173 (1991).

[14] Fadi Sun, Jinwu Ye, Wu-Ming Liu, Quantum magnetism of spinor bosons in optical lattices with synthetic non-Abelian gauge fields at zero and finite temperatures, Phys. Rev. A 92, 043609 (2015).

[15] Fadi Sun, Jinwu Ye, Wu-Ming Liu, Hubbard model with Rashba or Dresselhaus spin-orbit coupling and Rotated Anti-ferromagnetic Heisenberg Model, arXiv:1601.01642,

to be published in Phys. Rev. B.

[16] In fact, the Wilson ratio $R_w = (\frac{k_B T}{\Delta})^2$ in the $\Delta \gg k_B T$ regime here is identical not only as that in 2d TQPT driven by the collsions of Dirac fermions in a honeycomb lattice in[10], but also as that in the Rotated Ferromagnetic Heisenberg model (RFHM) in[14], Rotated Anti-ferromagnetic Ferromagnetic Heisenberg model (RAFHM) in[15] where the Wilson ratio is defined as the ratio of the conserved magnetic susceptibility over the specific heat. It is not known why it is identical in all these un-related models.

[17] For a review, see Turner, A. M. & Vishwanath, A. Beyond Band Insulators: Topology of Semi-metals and Interacting Phases. Preprint at http://arxiv.org/abs/1301.0330 (2013).

[18] Su-Yang Xu, *et.al* and M. Zahid Hasan, Discovery of a Weyl fermion state with Fermi arcs in niobium arsenide, NATURE PHYSICS — VOL 11 — SEPTEMBER 2015 — www.nature.com/naturephysics.

[19] Su-Yang Xu, *et.al*, M. Zahid Hasan, Discovery of a Weyl fermion semimetal and topological Fermi arcs, Science 349, 613 (2015);

[20] L. X. Yang, *et.al* and Y. L. Chen, Weyl semimetal phase in the non-centrosymmetric compound TaAs, NATURE PHYSICS — VOL 11 — SEPTEMBER 2015 — www.nature.com/naturephysics.

[21] B. Q. Lv, *et.al* and H. Ding, Observation of Weyl nodes in TaAs, NATURE PHYSICS — VOL 11 — SEPTEMBER 2015 — www.nature.com/naturephysics.

[22] Ling Lu, *et.al*, John D. Joannopoulos and Marin Soljacic, Experimental observation of Weyl points, Science 349, 622 (2015).

[23] Yu Yi-Xiang, Fadi, Sun, Jinwu Ye and Ningfang Song, Searching new topological superfluids and phase transitions with spin-orbit coupled fermions in an optical lattice, arXiv:1609.06554.

[24] A.A. Soluyanov, D. Gresch, Z. Wang, Q. Wu, M. Troyer, X. Dai, and B. Andrei Bernevig, Type-II Weyl Semimetals, Nature (London) 527, 495 (2015).

[25] Yi-Xiang Yu, Jinwu Ye, Wu-Ming Liu, Coherent lengths in attractively interacting Fermi gases with Spin-orbit Couplings, Phys. Rev. A 90, 053603 (2014).

[26] We think that the title "Type-II Weyl Semimetals " in Ref.[24] maybe mis-leading, because Type II Weyl fermions lead to a metal instead of a semi-metal.

[27] Zhijun Wang, *et.al* and B. Andrei Bernevig, MoTe2: A Type-II Weyl Topological Metal.

[28] A. Tamai, *et.al* and F. Baumberger, Fermi Arcs and Their Topological Character in the Candidate Type-II Weyl Semimetal MoTe2, PHYSICAL REVIEW X 6, 031021

(2016).

29. Lianghui Huang, *et.al*, Experimental realization of a two-dimensional synthetic spin-orbit coupling in ultracold Fermi gases, Nature Physics 12, 540-544 (2016).

30. Zengming Meng, *et.al*, Experimental observation of topological band gap opening in ultracold Fermi gases with two-dimensional spin-orbit coupling, arXiv:1511.08492.

31. Michael L. Wall, *et.al*, Synthetic Spin-Orbit Coupling in an Optical Lattice Clock, Phys. Rev. Lett. 116, 035301 (2016).

32. Zhan Wu, *et.al*, Realization of Two-Dimensional Spin-orbit Coupling for Bose-Einstein Condensates, Science 354, 83-88 (2016).

33. Nathaniel Q. Burdick, Yijun Tang, and Benjamin L. Lev, Long-Lived Spin-Orbit-Coupled Degenerate Dipolar Fermi Gas, Phys. Rev. X 6, 031022 C Published 17 August 2016.

34. Medley, P., Weld, D. M., Miyake, H., Pritchard, D. E. & Ketterle, W. Spin Gradient Demagnetization Cooling of Ultracold Atoms. *Phys. Rev. Lett.* **106**, 195301 (2011).

35. Sugawa, S. *et al.* Interaction and filling-induced quantum phases of dual Mott insulators of bosons and fermions. *Nat. Phys.* **7**, 642 (2011).

36. Kinast, J. *et al.* Heat Capacity of a Strongly Interacting Fermi Gas. *Science* **307**, 1296 (2005).

37. Ku, M. J. H. *et al.* Revealing the Superfluid Lambda Transition in the Universal Thermodynamics of a Unitary Fermi Gas. *Science* **335**, 563 (2012).

38. Gemelke, N., Zhang X., Huang C. L., and Chin, C. In situ observation of incompressible Mott-insulating domains in ultracold atomic gases, Nature (London) **460**, 995 (2009).

39. Leticia Tarruell, Daniel Greif, Thomas Uehlinger, Gregor Jotzu and Tilman Esslinger, Creating, moving and merging Dirac points with a Fermi gas in a tunable honeycomb lattice, Nature483, 302-305 doi:10.1038/nature10871.

40. Fadi Sun, Jinwu Ye, Wu-Ming Liu, Quantum incommensurate Skyrmion crystal phases and Commensurate to Incommensurate transitions of cold atoms and materials with spin orbit couplings, arXiv:1502.05338.

41. Fadi Sun, Jinwu Ye, Wu-Ming Liu, Classification of magnons in Rotated Ferromagnetic Heisenberg model and their competing responses in transverse fields, Phys. Rev. B 94, 024409 (2016).

42. Petr Horava, Stability of Fermi Surfaces and K Theory, PRL 95, 016405 (2005); N. Read, Compactly-supported Wannier functions and algebraic K-theory, arXiv:1608.04696.

43. The leading anisotropic dynamic exponents associated with the bosonic analog of the Type II Weyl fermions happen in the Rotated Ferromagnetic Heisenberg model (RFHM) in a longitudinal Zeeman field[40], but not in a transverse field[41].

44. M. Levin and X. G. Wen, Phys. Rev. Lett. **96**, 110405, (2006); A. Kitaev and J. Preskill, Phys. Rev. Lett. **96**, 110404 (2006).

45. C. Holm and W. Janke, J. Phys. A 27, 2553 (1994); M. H. Lau and C. Dasgupta, Phys. Rev. B 39, 7212 (1989); M. Kamal and G. Murthy, Phys. Rev. Lett. 71, 1911 (1993).

46. J. Ye, Y. B. Kim, A. J. Millis, B. I. Shraiman, P. Majumdar, and Z. Tešanović, Phys. Rev. Lett. **83**, 3737 (1999).